Heat transfer, thermocapillary convection and interface shapes in floating zone crystal growth with a magnetic field

G. Chen, B. Roux

HEAT TRANSFER, THERMOCAPILLARY CONVECTION AND INTERFACE SHAPES IN FLOATING ZONE CRYSTAL GROWTH WITH A MAGNETIC FIELD

GANG CHEN*AND BERNARD ROUX†
Institut de Mécanique des Fluides, CNRS-UMR 34
1, rue Honnorat, 13003 Marseille, France

Abstract

A numerical method is developped to study heat transfer and thermocapillary convection in the melt in floating zone crystal growth. The model for calculation is constructed of cylindrical coordinates with a symmetrical axis. The appropriate heat, mass and momentum transfer equations in primitive form are approximated using finite difference method on semi-staggered grids. The unknown melting and solidification fronts and melt/gas interface are calculated using boundary-fitted curvilinear coordinate system. Both solutions in the case of conduction heat transfer only and thermocapillary convection are presented. The effects of growth rate and externally applied magnetic field on the temperature and flow fields, the zone length and the shapes of the melting and solidification fronts are demonstrated.

Introduction

The use of microgravity environment and magnetic field to control the flow field, heat and mass transfer during the growth of large-diameter semiconductor crystals from the melt in floating zone system has received a great deal of attention in the recent years. Due to the absence of hydrostatic pressure, the stability of melt/gas meniscus is increased and its deformation is reduced which is particularly important because it opens the way to processing methods in microgravity with liquid/fluid interfaces too large to be maintained with earth's gravity. Suppression of buoyancy-driven convection in the melt under microgravity conditions is not enough to guarantee the growth of compositionally uniform crystals; intense thermal driven flow due to the variation of surface tension with temperature is still present. Owing to the large electrical conductivity of semiconductor melts, the application of a magnetic field can suppress flow across magnetic field lines, and hence alters the entire melt motion, through the presence of the electromagnetic Lorentz force. Thus, it might be expected that with suppression of the melt motion by the magnetic field, the heat and mass transfer would be such as to produce better crystals. Recent microgravity experiment of germanium crystal growth by floating zone method, GEZON, during the Photon mission in the Zona-4M furnace has been the above mentioned purpose.

In a previous paper [1], we reported numerical results of hydrodynamics of the melt associated with the GEZON experiment. The calculation of the zone shape and the thermocapillary convection in the melt operating under microgravity conditions has been performed by using NEKTON code. The deformation of the melt/gas interface has not been included. This paper describes a finite difference method for solution of the hydrodynamic thermocapillary model of floating zone process. The model includes axisymmetric, steady-state convection in the melt, heat transfer in the melt, feed crystal and solidifying crystal and the determination of the shapes of the melt/solid and melt/gas interfaces from interfacial energy and momentum balances, respectively. Thus the present model comprises a rather complex free-boundary problem for the field variables and interface shapes.

During the past ten years, several coupled asymptotic/numerical approaches and direct numerical simulations have been devoted to solution of the coupled system for floating zone process [2–4]. Many of these followed the early work of Duranceau & Brown [2] who considered a conduction-dominated heat transfer model. Many numerical algorithms for the solution of free-boundary problems used domain transformation technique. Different numerical techniques, say, finite difference method, or finite element method, have been applied to solve transformed equations. The discretization by the finite difference method is used in this work. The use of the boundary-fitted coordinate system in this procedure is a very important element. This is because the boundary-fitted coordinate system easily enables us to calculate the grid points if the coordinates of the boundaries are given. The procedure we follow, to some extent, is similar to that of Lan & Kou [4], but we solve governing equations in terms of primitive variables (velocity and pressure), instead of stream function and vorticity. Although the latter formulation avoids problems associated with the numerical calculation of the pressure field, it is much easier to treat the melt/gas interface boundary conditions in terms of primitive variables as the pressure field is computed directly from solution procedure. The numerical procedures based on the primitive variables can also more easily be generalized to three dimensions. Because of limited space, this paper can only give an overview of the numerical method and results of the analysis for the floating zone associated with the GEZON experiment. A more complete report about the

*Postdoctoral Fellow
†Directeur de Recherche au CNRS

numerical implementation will be presented elsewhere [6].

Model Formulation

We considere the model floating zone crystal growth shown in figure 1, with (r, θ, z) as the cylindrical coordinates. The system is considered to be axisymmetric so that there is no dependence on the azimuthal coordinate, θ, in the dependent variables or boundary conditions. We define a coordinate system translating with the interfaces. The so-called quasi-stationary approach is adopted in this analysis, which by mass conservation implies $V_c R_c^2 = V_f R_f^2$, where V is the pulling rate, R the radius, the subscrips c and f denote crystal and feed rods, respectively. A static, uniform magnetic field is applied externally in the direction of crystal growth, $\vec{B} = B_0 \vec{e_z}$, where B_0 is the applied magnetic induction. We assume that both magnetic Reynolds number and magnetic Prandtl number are small, so that the magnetic field produced by any electric currents in the melt, crystal or feed rod can be ignored. Futhermore, the electrical conductivity of the crystal and feed rods are neglected and the crystal and feed rods are traited as an electrical insulator. Thus in the present axisymmetric analysis, the electrical field vanishes everywhere and the Lorentz force reduces to a systematically damping factor $-\sigma_e B_0^2 u \vec{e_r}$, where σ_e is the electrical conductivity of the melt and u the radial component of velocity.

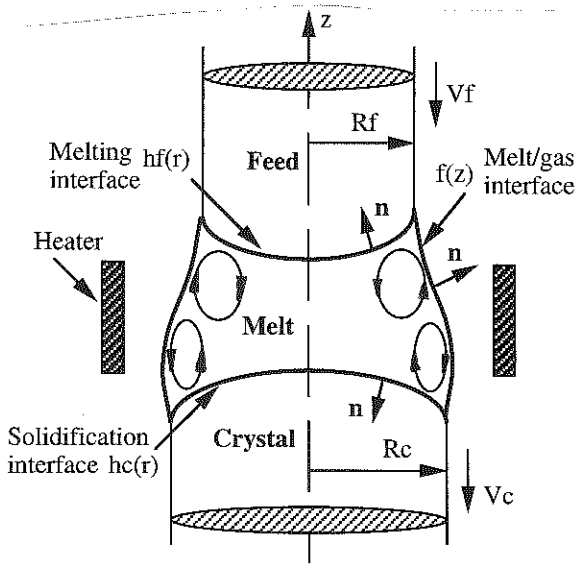

Fig.1 Schematic of the floating zone crystal growth process.

Let $\vec{u} = u\vec{e_r} + w\vec{e_z}$ be the velocity, p be the pressure and T be the temperature, then the following equations describe the heat transport in the melt, feed rod and crystal, and momentum and mass conservation in the melt:
Melt(l):

$$\rho_l \vec{u} \cdot \nabla \vec{u} = -\nabla p + \mu \nabla^2 \vec{u} - \sigma_e B_0^2 u \vec{e_r} + \rho_l \beta \vec{g}(T_l - T_m), \quad (1)$$

$$\nabla \cdot \vec{u} = 0, \quad (2)$$

$$\rho_l C_p \vec{u} \cdot \nabla T_l = \kappa_l \nabla^2 T_l. \quad (3)$$

Crystal(c) and feed rod(f):

$$\rho_i C_p V_i \frac{\partial T_i}{\partial z} + \nabla \cdot (\kappa_i \nabla T_i) = 0, i = c, f \quad (4)$$

The thermal boundary conditions are as follows:
Along the centerline of symmetry,

$$\frac{\partial T}{\partial r} = 0. \quad (5)$$

At the melting and solidification fronts,

$$\kappa_l \vec{n_i} \cdot \nabla T_l - \kappa_s \vec{n} \cdot \nabla T_i = -\rho_s \mathcal{L} V_i \vec{n_i} \cdot \vec{e_z}, i = c, f \quad (6)$$

$$T = T_m. \quad (7)$$

At the lateral surfaces of the feed rod, melt and crystal,

$$-\kappa_i \vec{n_i} \cdot \nabla T_i = h(T_i - T_a(z)) + \varepsilon_i \sigma (T_i^4 - T_a(z)^4), i = c, f, l \quad (8)$$

At the sample ends,

$$T(z = 0) = T_0, T(z = L) = T_L. \quad (9)$$

Equation (6) represents the energy conservation across the melt/solid interfaces and Eq.(7) the equilibrium condition. Eq.(8) describes the heat exchange between the sample and the surrounding by convection and radiation. The condition of specified temperatures at the sample ends (Eq.(9)) can be replaced by heat flux condition.

The fluid flow boundary conditions are as follows:
Along the centerline of symmetry,

$$u = \frac{\partial w}{\partial r} = 0. \quad (10)$$

At the melting and solidification fronts,

$$u = 0, w = -\rho_s / \rho_l V_i, i = c, f \quad (11)$$

At the melt/gas interface,

$$\vec{u} \cdot \vec{n} = 0, \quad (12)$$

$$\sum_{i,j=1}^{2} \sigma_{ij} n_j n_i = K\gamma - P_a + \lambda, \quad (13)$$

$$\sum_{i,j=1}^{2} \sigma_{ij} n_j t_i = \vec{t} \cdot \nabla \gamma, \quad (14)$$

Equation (12) is the kinematic condition. Eqs.(13) and (14) represent, respectively, the normal and tangential forces balances. The constant λ in Eq.(13) is a reference pressure. To set the value of λ, we need to impose an additional condition. In simulated floating zone systems formed by drops captive between two parallel, coaxial solid disks, the drop volume is given *a priori* and is conserved, this volume conservation constraint is used to

set the reference pressure. In a floating zone with solidification, however, the actual volume of the melt is not known *a priori*, because it depends on the interaction of heat transfer and capillarity. The reference pressure is determined by the additional constraint that the contact angle formed at the junction of the crystal, melt and ambient has a specified value, ϕ; this condition is written as,

$$\frac{df}{dz} = tan\phi, \tag{15}$$

where $f(z)$ is a function describing the melt/gas meniscus shape.

Finally, when the liquid/gas interface meets the melting and solidifying interfaces, we have the following contact line conditions,

$$f(z = h_c(r = R_c)) = R_c, f(z = h_f(r = R_f)) = R_f. \tag{16}$$

Summarying, for the floating zone system shown in Fig.1, the governing equations are (1-4) subject to the boundary conditions (4-14). Eqs.(15) and (16) set the reference pressure and establish the trijunction of the melt/solid and melt/gas surfaces.

Solution Method

Since the interface is one of most important features in the present problem, a boundary-fitted curvilinear coordinate system with its coordinate lines coinciding with the interface contour is used. This method [7] avoids inaccurancy and irregularity due to interpolation near the curved boundaries. It also allows the contracted coordinate lines in the regions where the higher temperature and velocity gradients are expected, for example, in the vicinity of interface boundaries. Following to Thompson et al. [7], the boundary-fitted coordinate system $r = r(\xi, \eta)$ and $z = z(\xi, \eta)$ are defined as the solution of the quasi-elliptic equations,

$$g_{11}r_{\xi\xi} - 2g_{12}r_{\xi\eta} + g_{22}r_{\eta\eta} + J^2(Pr_\xi + Qr_\eta) = 0, \tag{17}$$

$$g_{11}z_{\xi\xi} - 2g_{12}z_{\xi\eta} + g_{22}z_{\eta\eta} + J^2(Pz_\xi + Qz_\eta) = 0, \tag{18}$$

where $g_{11} = r_\eta^2 + z_\eta^2$, $g_{12} = r_\xi z_\eta + r_\eta z_\xi$, $g_{22} = r_\xi^2 + z_\xi^2$, $J = r_\xi z_\eta + r_\eta z_\xi$, $P(\xi, \eta)$ and $Q(\xi, \eta)$ are functions of the control of spacing of the coordinate lines, the subscripts ξ and η denote the partial derivative with respect to ξ and η, respectively. Equations (17,18) are discretized by the second-order centered finite-difference approximation for the derivatives and solved by the usual SOR method. Figure 2 illustrates an example of coordinate transformation of the physical plane (r, z) into a fixed rectangular computational plane (ξ, η) with uniform grids.

The governing equations (1-4) and boundary conditions (5-16) are transformed into the computational domaine (ξ, η). The temperature in each phase and the velocity components in the melt are defined on the grid points and the pressure in the melt is defined in the mesh centers, so that the semi-staggered grids are used in the computation. The avantages and disavantages associated with this kind of grid in comparison with the widely used MAC staggered grids are discussed in [6]. The transformed differential equations and boundary conditions are approximated, whenever it is possible, by the second-order centered finite-difference formulae. Discretized equations (1,2,10-12 and 14) are written for the flow field in the melt and (3-9) for the temperature field in the whole domain. Each of resulting nonlinear algebraic equations is solved by Newton's method. For an appropriate ordering of the grid points and unknowns in the computational mesh, the associated Jacobian matrices are both banded. The required band LU factorization and triangular solvers at each Newton's iteration are performed by using the DGBFA/DGBSL sequence in the LINPACK subroutine library. One-dimensional discretized normal stress condition (13) with (15,16) are used to determine the meniscus shape. The melting and solidifying interfaces are obtained from the isothermal condition (7).

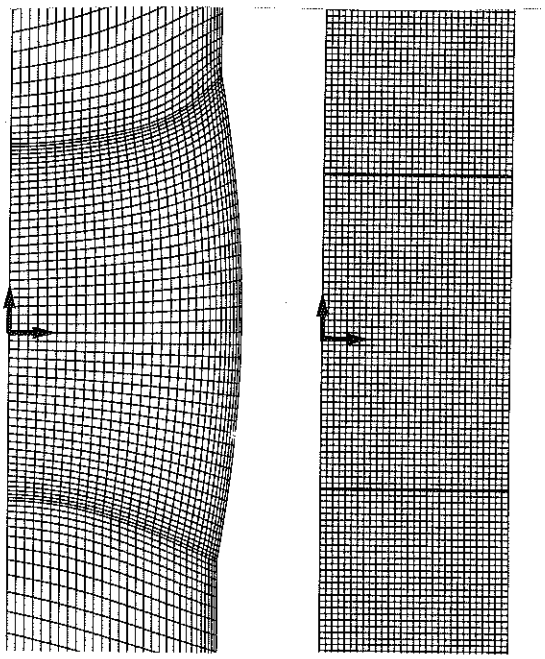

Fig.2 Example of coordinate transformation: (a) physical domain (r, z); (b) computational domain (ξ, η) with uniform grids. The arrow mark the melt/solid interfaces.

Given the initial estimate of the interface shapes and the field variables, the solution procedure is as follows:
(1) transform the physical plane into the rectangular computational plane;
(2) solve the equations for the temperature field in the crystal, melt and feed rod;
(3) solve the equations for the flow field in the melt;
(4) locate the new melting and solidifying interfaces;
(5) determine the new meniscus shape;
(6) update the interface shapes and the field variables.
All the calculations are repeated until the prescribed

convergence criteria are satisfied. The computations are carried out on the iPSC/860. Flow fields are displayed as stream functions computed by solving the appropriate Poisson equation using the velocity field from the calculation as input.

Results and Discussion

Table 1: Properties of Ge and operating parameters used in the calculations

sample radius	R	$0.75\ cm$
sample length	L	$13\ cm$
contact angle	ϕ	$10\ deg$
surface tension	γ	$605\ dyn/cm$ - 0.105 $\times(T - T_m)\ dyn/(cmK)$
thermal conductivity (melt)	κ_l	$0.38\ W/(cmK)$
thermal conductivity (solid)	κ_s	$0.18\ W/(cmK)$
density (melt)	ρ_l	$5.43\ g/cm^3$
density (solid)	ρ_s	$5.43\ g/cm^3$
heat capacity	C_p	$0.4\ J/(gK)$
volumetric latent heat	$\rho\mathcal{L}$	$2758.44\ J/cm^3$
melting point temperature	T_m	$1210\ K$
dynamic viscosity	μ	$5.973\times10^{-3}g/(cms)$
heat transfer coefficient	h	$1.1 \times 10^{-3}W/(cm^2K)$
emissivity (melt)	ε_l	0.18
emissivity (solid)	ε_s	0.5
pulling rate	V_p	$1.4\times10^{-4}cm/s$
electrical conductivity	σ_e	$1.52\times10^4/(\Omega cm)$

We present here only the computations on the flows driven by surface-tension gradients; buoyancy-driven flows are not considered. The thermophysical properties of germanium and the operating parameters used in the calculations are listed in the Table 1. Although the numerical scheme is able to test different heater configuration (Equ.(8)), we adopted an ambient temperature profile as shown in Figure 3, which is a function of z. This specific heater profile is based on the ground-based measurement (Senchenkov, private communication). Note that $T_a(z)$ is not symmetric about the middle plane; the temperature at the bottom crystal being higher than that at the top feed rod. We shall see below that this asymmetric heating will result in the asymmetry of flow field.

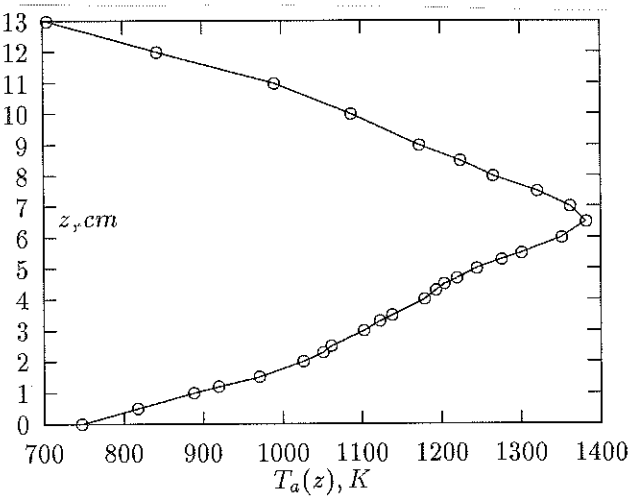

Fig.3 Heater temperature profile, $T_a(z)$, used in the computations

Figures 4a and 4b illustrate the calculated results with no crystal growth based on respectively conduction heat transfer only and thermocapillary convection. As shown, the surface temperature difference in the melt, ΔT_{max}, in the latter case is smaller than that in the former case. This is due to the fact that convective flow moves the hotter melt (at the middle plane) along the free surface toward the melt/solid interfaces and returns the colder melt along the centerline toward the hot spot. Therefore, heat transfer to the melt/solid interfaces is enhanced near the free surface but decreased near the centerline. Consequently, the melt zone due to the thermocapillary convection is longer at the free surface and shorter at the centerline; the height being respectively $1.76cm$ and $1.27cm$. However, because of small Prandtl number of the melt of Ge, heat transfer is conduction-dominated, at least in the range of operating parameters used herein, the difference of the zone shapes between the two cases is not significant. It might be expected that the difference would become important for the larger Prandtl number melt. Since the heat transfers into the melt zone from heater by radiation and convection (Eqs.(8)), the surface temperature gradients and resulting motion in the melt depend substantially on the heater temperature profile, $T_a(z)$. The flow field shown in Figure 4b based on the above $T_a(z)$ demonstrates the asymmetry in the motion with the bottom flow cell being more intense and the top cell being confined to the upper corner. The maximum and minimum stream functions, which are located respectively at the centers of top and bottom cells, are $\psi_{max} = 0.043cm^3/s$ and $\psi_{min} = -0.087cm^3/s$. The fastest surface flow, associated with the top cell is $w_{max} = 2.08cm/s$, and that the bottom cell $w_{min} = -2.78cm/s$. The velocity profile along the free surface is shown in Figure 5. As shown, very high surface velocity gradients are located in the vicinity of the melt/solid interfaces which need a very fine mesh in these regions in the computation.

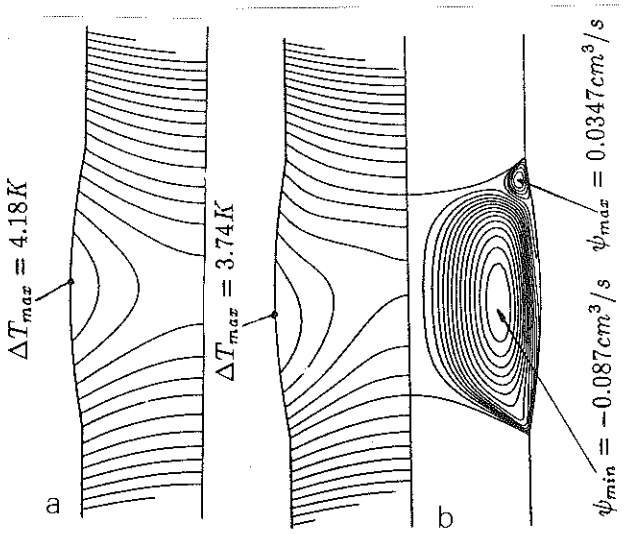

Fig.4 Calculated results with no crystal growth based on: (a) conduction; (b) thermocapillary convection. $\Delta\psi = (\psi_{max} - \psi_{min})/20$, $\Delta T_{melt} = \Delta T_{max}/6$ and $\Delta T_{solid} = 3\Delta T_{melt}$. This will be so in the figures to follow.

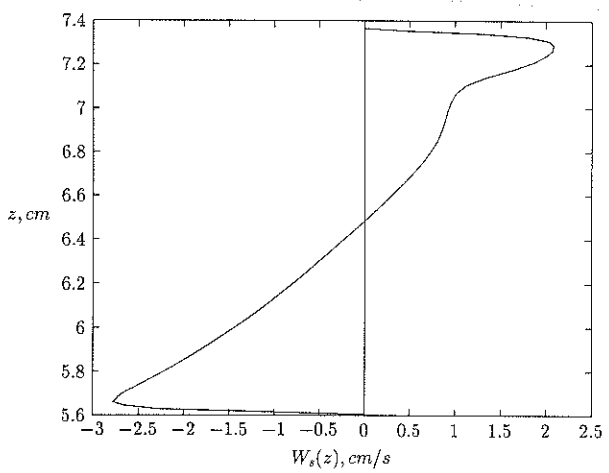

Fig.5 Velocity profile along the melt/gas interface

In Figure 6 we examine the results for varing V_p, the growth rate. The introduction of latent heat effects and the translation of the solid rods caused by crystal growth cause the molten zone to translate down relative to the heater. The melt/solid interfaces are affected such that the melting (upper) interface is drawn further into the heater, thereby increasing its deflection and the solidification (lower) interface is pushed further outside the heater and the temperature field becomes more uniform, thereby flattening the interface. The flow structures are similar to that without growth. But due to the shift of overall position of the melt zone toward crystal, the top flow cell becomes further smaller and weaker, while the bottom one becomes larger and stronger.

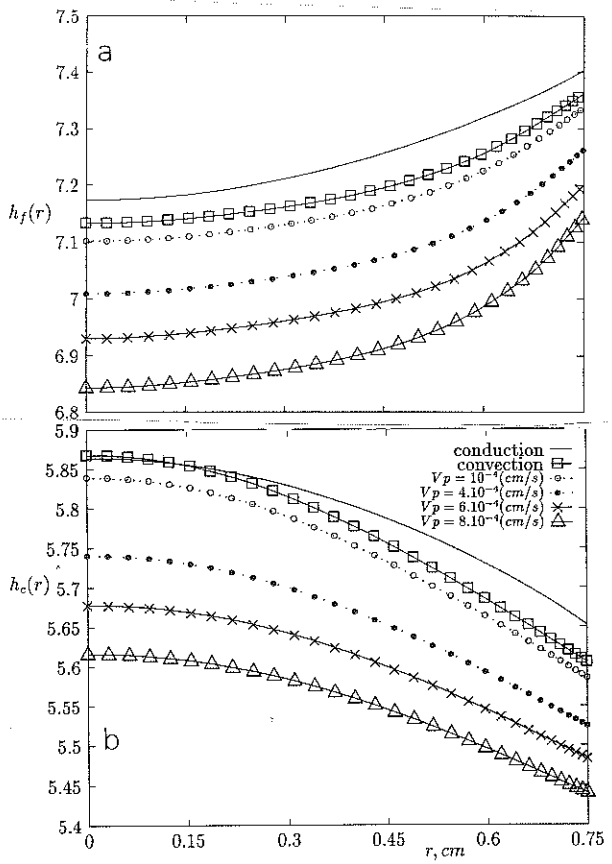

Fig.6 Effect of growth rate on the melting (a) and solidifying (b) interface shapes.

The effect of magnetic field on the temperature and flow fields are shown in Figure 7. The magnetic induction, B_0, are $0.1Tesla$ and $0.3Tesla$ in Figs.7a and 7b, respectively. As the result of damping effect througth the Lorentz force, the intensity of return flow in the radial direction is reduced. Thus, the overall melt motion is damped and convective heat transfer becomes smaller. Since the Lorentz force is proportional to the radial component of velocity, the higher the radial velocity is, the stronger the damping effect becomes. Therefore, as shown, the asymmetry of the melt motion is not so significant in comparison with that without magnetic field and with increasing magnetic induction the melt motion tends to be symmetric with respect to the heater. The variation of the maximum and minimum stream functions with the magnetic induction is shown in Figure 8. Increasing of magnetic induction first increases the top flow cell up to $B_0 = 0.1T$ and then decreases it. The bottom flow cell is always decreased with increasing B_0.

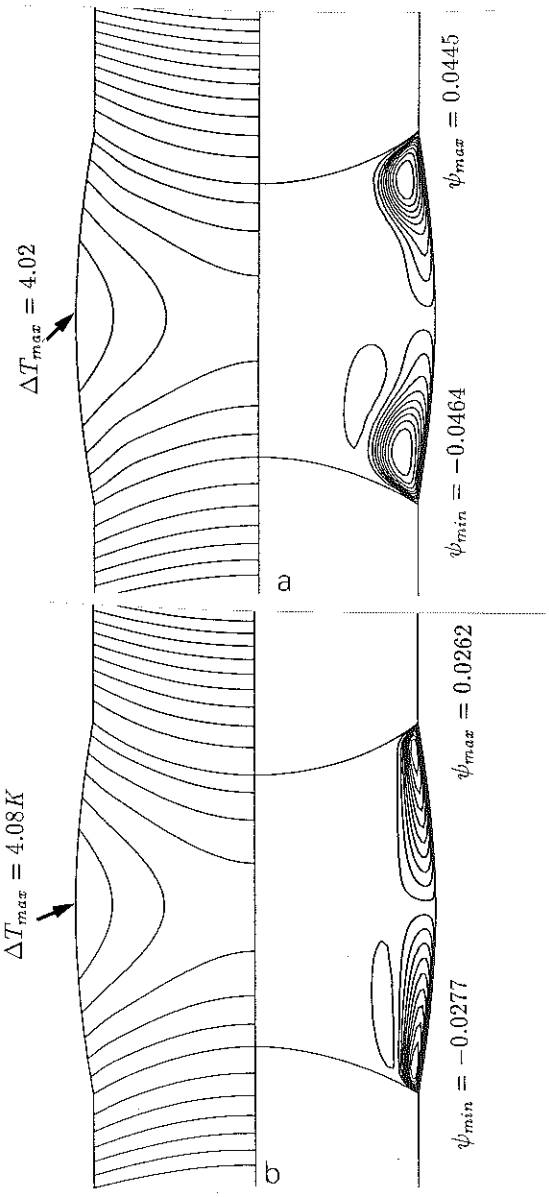

Fig.7 Effect of magnetic field on the temperature and flow fields: (a) $B_0 = 0.1T$; (b) $B_0 = 0.3T$.

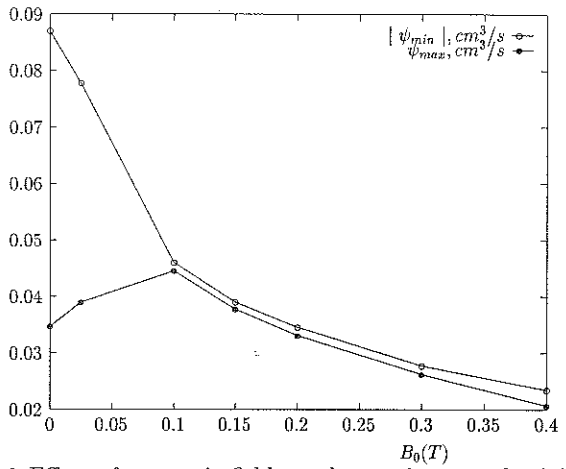

Fig.8 Effect of magnetic field on the maximum and minimum stream functions.

The magnetic effect on the molten zone length at the surface and centerline is illustrated in Figure 9. Although the convective heat transfer is decreased by magnetic damping, its effect on the shape of melt/solid interfaces is not significant. As mentioned above, this is due to very small Prandtl number of the melt of Ge; the coupling between flow field and temperature filed being small. In fact the limiting case corresponds to the conduction solution.

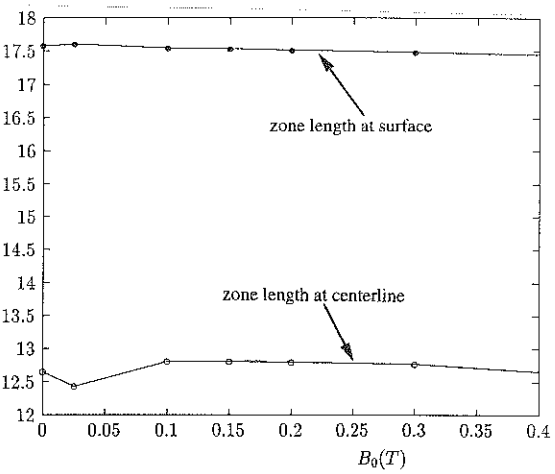

Fig.9 Effect of magnetic field on the molten zone length: (a) at surface; (b) at centerline.

Conclusion

We have presented a finite difference method for solution of the hydrodynamic thermocapillary model of floating zone process. It has been shown that the thermocapillary convection tends to reduce the maximum surface temperature, increase the convexity of the melt/solid interfaces and reduce the stability of the melt zone. Increasing in the growth rate shifts the overall position of the melt zone toward the crystal and causes the melt/feed and melt/crystal interfaces to be more and less convex, respectively. Intense thermocapillary convection is damped by a uniform axial magnetic field. When magnetic induction is increased, the convection intensities are much more reduced, the temperature fields are less distorted, the convections in the melt are concentrated into a small region near the free surface and the cell centers move toward the melt/solid interfaces. For small Prandtl number of semiconductor melts, like germanium and silicon, the effect of magnetic field on the melt/solid interfaces has been found small; limiting case corresponding to the conduction heat transfer.

Finally, the numerical algorithm presented here is very general and not limited to axisymmetric floating zone system, it can be easily applied to solution of many free-boundary problems.

Acknowledgments—We would like to thank Drs. Camel, Senchenkov and Prof. Moreau for contributions to this work. This research was supported by the Centre National d'Etudes Spatiales(CNES). G. Chen received a Post-Doctoral fellowship from the CNES which is gratefully acknowledged. Computations were performed on the Intel iPSC/860 at the IMFM.

References

[1] Chen, G., Roux, B., Camel, D, Tison, P., Garandet, J.P., Favier, J.J., Senchenkov A.S. and Moreau, R, 1994 Numerical Study of GEZON Experiment, *Microgravity sci. technol.*, VII/2.

[2] Duranceau, J.L. and Brown, R.A., 1986 Thermal-Capillary Analysis of Small-Scale Floating Zones: Steady-State Calculations, *J. Crystal Growth*, **75**, 365-389.

[3] Duranceau, J.L. and Brown, R.A., 1988 Finit Element Analysis of Melt Convection and Interface Morphology in Earthbound and Microgravity Floating Zones, *Proc. of the Third Int. Coll. on Drops and Bubbles.*

[4] Young, G.W. and Chait, A., 1991 Steady-State Thermal-Solutal Convection and Diffusion in a Simulated Float Zone, in *Low-Gravity Fluid Dynamics and Transport Phenomena*, Edited by J.N. Koster and R. L. Sani, **130**, 119-157.

[5] Lan, C.W. and Kou, S., 1991 Heat Transfer, Fluid Flow and Interface Shapes in Floating-Zone Crystal Growth, *J. Crystal Growth*, **108**, 351-366.

[6] Chen, G. and Roux, B. Finite-difference solution of heat transfer and fluid flow during melting and solidification with solid/liquid phase change and free liquid/gas interface, in preparation.

[7] Thompson, J.F., Thames, F.C. and Mastin, C.W., Boundary-fitted curvilinear coordinate systems for solution of partial differential equations on fileds containing any number of arbitrary 2-dimensional bodies, *NASA Report NASA-CR-2729*, July 1977.